Article

Current Biology

Grid cell disruption in a mouse model of early Alzheimer's disease reflects reduced integration of self-motion cues

Highlights

- Grid cell disruption in J20 mice reflects reduced integration of self-motion cues
- J20 grid cells are unstable in the center of the environment
- J20 grid cells exhibit reduced theta rhythmicity and theta phase precession
- J20 grid cells more strongly align parallel to the spatial environment's borders

Authors

Johnson Ying, Antonio Reboreda, Motoharu Yoshida, Mark P. Brandon

Correspondence

mark.brandon@mcgill.ca

In brief

The mechanisms that underlie deficits in path integration in early Alzheimer's disease (AD) remain unclear. Ying et al. show in a transgenic amyloid mouse model of AD that disrupted grid cell coding reflects reduced integration of self-motion cues, providing evidence that grid cell impairments underlie path integration deficits during early AD.

Ying et al., 2023, Current Biology *33*, 2425–2437
June 19, 2023
https://doi.org/10.1016/j.cub.2023.04.065

CellPress

Current Biology

CellPress

Article

Grid cell disruption in a mouse model of early Alzheimer's disease reflects reduced integration of self-motion cues

Johnson Ying,[1,2] Antonio Reboreda,[3,4] Motoharu Yoshida,[3,4,5] and Mark P. Brandon[1,2,6,*]
[1]Department of Psychiatry, Douglas Hospital Research Centre, McGill University, Montreal, QC H4H 1R3, Canada
[2]Integrated Program in Neuroscience, McGill University, Montreal, QC H3A 0G4, Canada
[3]German Center for Neurodegenerative Diseases (DZNE), Magdeburg 39120, Germany
[4]Leibniz Institute for Neurobiology (LIN), Magdeburg 39120, Germany
[5]Center for Behavioral Brain Sciences (CBBS), Magdeburg 39106, Germany
[6]Lead contact
*Correspondence: mark.brandon@mcgill.ca
https://doi.org/10.1016/j.cub.2023.04.065

SUMMARY

Converging evidence from human and rodent studies suggests that disrupted grid cell coding in the medial entorhinal cortex (MEC) underlies path integration behavioral deficits during early Alzheimer's disease (AD). However, grid cell firing relies on both self-motion cues and environmental features, and it remains unclear whether disrupted grid coding can account for specific path integration deficits reported during early AD. Here, we report in the J20 transgenic amyloid beta (Aβ) mouse model of early AD that grid cells were spatially unstable toward the center of the arena, had qualitatively different spatial components that aligned parallel to the borders of the environment, and exhibited impaired integration of distance traveled via reduced theta phase precession. Our results suggest that disrupted early AD grid coding reflects reduced integration of self-motion cues but not environmental information via geometric boundaries, providing evidence that grid cell impairments underlie path integration deficits during early AD.

INTRODUCTION

Grid cells in the medial entorhinal cortex (MEC) fire in multiple spatial locations to form a periodic hexagonal array that spans two-dimensional space.[1–3] This periodic code is implicated in path integration, a cognitive function that requires the integration of self-motion cues to maintain one's sense of location relative to a starting point in space.[4–7] Both grid cell and path integration impairments are sensitive markers of pathological decline during early Alzheimer's disease (AD) in human subjects and mouse models of pathology.[7–13]

However, it remains unclear whether early grid impairments result from disrupted processing of self-motion cues or environmental information provided by external landmarks and geometric boundaries. Self-motion cues constitute necessary inputs that maintain grid representations in healthy animals.[2,14–25] Yet, geometric boundaries also exert significant influences over grid coding, particularly in rectilinear environments where grid representations scale proportionally to manipulations along the borders.[26] Furthermore, deformed grid hexagonal symmetry in asymmetrical enclosures such as trapezoids demonstrates the degree to which geometric boundaries compete with self-motion cues to generate grid firing.[27]

To distinguish whether early AD grid cell impairments reflect increased noise across the network or a specific deficit in processing self-motion cues over landmark information provided by environmental boundaries, we analyzed our *in vivo* electrophysiological dataset of MEC neurons recorded in the J20 transgenic amyloid beta (Aβ) mouse model of early AD that expresses a mutant form of human amyloid precursor protein (APP)—referred to here as "APP mice."[11,12]

RESULTS

Adult APP grid cells are spatially unstable in the center of the environment

We analyzed 4,524 MEC neurons from 38 APP transgenic and 30 non-transgenic (nTG) littermates as they foraged for water droplets in a 75-cm-square arena that had two cue cards on the north and west walls (STAR Methods section neural recordings; Figure S1; Table S1).[12] Mice were recorded between the ages of 3 and 7 months, time points corresponding to the early stages of pathology prior to the expression of widespread Aβ plaques (detailed pathology description in STAR Methods section experimental model and subject details). Mice were categorized into two age groups: young mice between 3 and 4.5 months of age (APP-y and nTG-y) and aged mice between 4.5 and 7 months of age (APP-a and nTG-a). Cells with gridness scores (a measure of hexagonal spatial periodicity in the rate map) higher than the 99th percentile of a shuffled distribution (a gridness score above 0.54) were characterized as grid cells (STAR Methods section grid cell selection).

To quantify the spatial stability of grid cells in the center of the environment, we divided the spatial arena into "wall" or "center"

regions. The wall length was selected to be 12 cm, corresponding to the body length of a mouse, and approximately divides the wall and center regions into equal surface areas (Figure 1A). Spatial stability was analyzed in two different ways. Briefly, a time-partitioned analysis split the first 30 min of each grid cell recording into two 15-min partitions. Alternatively, an occupancy-partitioned analysis split the entire recording into two maps, where the occupancies in each spatial bin were the same. Higher correlation scores between wall or center partitions indicate higher spatial stability (STAR Methods section spatial stability analysis). Both methods revealed greater center instability only in APP-a grid cells (Figures 1B–1D; n = 36, 64, 30, and 37 cells for nTG-y, nTG-a, APP-y, and APP-a, respectively). In contrast, wall stability scores were not significantly different across groups (Figures 1B–1D). We repeated our analysis in an unbiased manner by incrementally decreasing the size of the center region while subsequently increasing the size of the wall region (Figure S2). On each iteration, the outermost pixel layer along the x and y dimensions of the center region was added to the innermost pixel layer of the wall region (Figure S2). In both time-partitioned and occupancy-partitioned analyses, APP-a center stability was significantly lower than other groups across multiple conditions. In contrast, wall stability generally remained nonsignificant across groups until more center spatial bins were included into the wall region (Figures S2A and S2B). Within each individual mouse group, APP-a grid cells also had the most instances where stability was lower in the center vs. the borders (Figures S2C and S2D). Greater instability toward the environmental center, where the sparsity of boundary-based landmark information necessitates the use of path integration to maintain a stable grid code, suggests that APP-a grid cells do not reliably process self-motion cues.

Adult APP grid cells exhibit fewer spatial Fourier spectral components

Previously, we reported a disruption in APP-a grid cell hexagonal symmetry.[12] However, it remains unclear whether these disrupted patterns reflect increased random noise in the network or qualitatively different underlying spatial geometries. To quantify potential structural differences of APP-a grid cells, we implemented a two-dimensional Fourier analysis to decompose a cell's spatial firing rate map into its basic spatial components (STAR Methods section generation of Fourier spectrums).[28] Grid cells typically had three components in the Fourier spectrum, which could be visualized as images of spatial axes facing specific orientations offset by 60°, such that the sum of all component images produced the firing rate map (Figure 2A). Similar to prior findings, grid cell Fourier components had distinct wavelengths (spacing between axes) where modules scaled by multiples ranging from 1.34 to 1.59 in all groups (Figure S3A).[26,28,29] To discount the inherent biases of grid cell selection criteria, we also applied the Fourier analysis to all recorded MEC cells. Most non-grid MEC cells typically had two Fourier components and adopted a square- or quadrant-like arrangement of spatial axes with angular offsets being multiples of 90° (Figure 2A; n = 768, 997, 720, and 1,318 cells for nTG-y, nTG-a, APP-y, and APP-a, respectively). We computed the polar autocorrelations of all recorded MEC cells by circularly shifting each cell's polar representation by 360° and found a noticeable decrease in 60° modulation but an increase in 90° modulation for APP-a mice (Figure 2B). These results suggest that APP-a spatial axes at the population level were less hexagonal and more quadrant-like.

Further quantification of Fourier component count revealed that APP-a mice had less 3-component grid cells. Grid cells in nTG-y, nTG-a, and APP-y mice generally had three significant Fourier components, while grid cells in APP-a mice had a similar number of cells with two or three components (Figure 2C). Most non-grid MEC cells had two significant Fourier components (Figure 2C). There was a higher percentage of 3-component grid cells than 3-component MEC cells in all groups except for APP-a mice (Figure 2D; nTG-y: $p < 0.001$, nTG-a: $p = 0.024$, APP-y: $p = 0.01$, APP-a: $p = 0.14$). On the other hand, there was a higher percentage of 2-component MEC cells than 2-component grid cells in nTG-y and APP-y mice, but not in nTG-a and APP-a mice (Figure 2D; nTG-y: $p = 0.005$, nTG-a: $p = 0.20$, APP-y: $p = 0.03$, APP-a: $p = 0.93$). These results suggest that only APP-a mice had both a larger percentage of 2-component grid cells and a smaller percentage of 3-component grid cells.

To determine the type of spatial alignment adopted by these 2- and 3-component cells, we computed the angular difference of neighboring Fourier components. Angular offsets in grid cell neighboring components were mostly 60° (and occasionally 90°) in nTG-y, nTG-a, and APP-y mice, but we observed similar percentages between 60° and 90° offsets in APP-a mice (Figures 2E and 2F; 60° ± 10°: nTG-y: 40%, nTG-a: 43%, APP-y: 40%, APP-a: 20%; 90° ± 10°: nTG-y: 11%, nTG-a: 12%, APP-y: 16%, APP-a: 22%). Furthermore, the ratio of 60°–90° was substantially reduced in APP-a grid cells (Figure 2E; [60° ± 10°]/[90° ± 10°]: nTG-y: 3.62, nTG-a: 3.61, APP-y: 2.48, APP-a: 0.91). APP-a grid cells had lesser instances of 60° angular offsets than other groups and greater instances of 90° angular offsets than nTG-a grid cells (Figure 2F). These results suggest that APP-a grid cell axes deviate from a 3-component hexagonal alignment and more strongly adopt a 2-component quadrant-like alignment.

Angular differences in the neighboring components of all MEC cells were predominantly multiples of 90° in all groups (Figure 2E). Relative to other groups, APP-a MEC cells had an ~60% decrease in 60° angular offsets and an ~15% increase in 90° angular offsets (Figure 2F; 60° ± 10°: nTG-y: 8.7%, nTG-a: 8.7%, APP-y: 8.7%, APP-a: 3.5%; 90° ± 10°: nTG-y: 25.5%, nTG-a: 24.9%, APP-y: 24.9%, APP-a: 28.6%). Statistically, APP-a MEC cells had lesser instances of 60° and greater instances of 90° angular offsets compared with other groups (Figure 2F).

Adult APP grid cell spatial axes align parallel to environmental borders

Our finding that the spatial stability of grid cells was not significantly reduced toward the arena's borders suggests that APP-a grid cells remained anchored to the environment despite a potential impairment of self-motion cue integration. To quantify this anchoring, we analyzed how hexagonal and quadrant-like spatial codes aligned to the environment's geometry. Most 2-component and 3-component cells adopted one of three alignment profiles (Figure 3A). Consistent with previous reports,

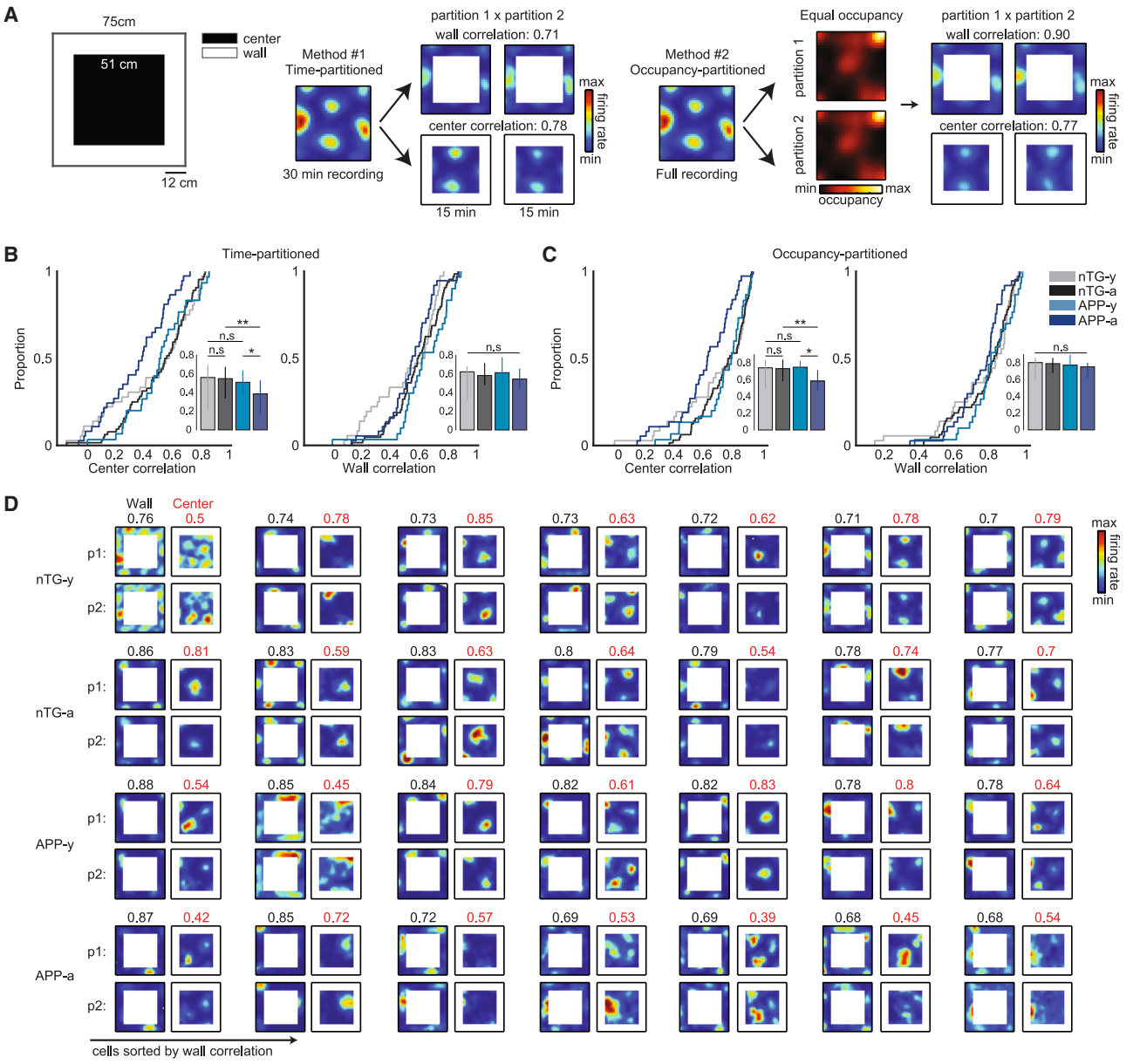

Figure 1. Adult APP grid cells are spatially unstable in the center of the environment

(A) The spatial arena was divided into "wall" and "center" regions. The wall length was 12 cm. Spatial stability was calculated via two methods. A time-partitioned analysis split the first 30 min of each grid cell recording into two 15-min partitions. An occupancy-partitioned analysis split the entire recording into two maps, where the occupancies in each spatial bin were the same. Higher correlation scores between wall or center partitions indicate higher spatial stability.

(B) Center stability is reduced in time-partitioned APP-a grid cell maps, but wall stability is preserved. Bars indicate medians and error bars show the 25th and 75th percentile, two-way ANOVA (center—age × genotype interaction: $F(1, 163) = 7.2$, $p = 0.008$; wall—age × genotype interaction: $F(1, 163) = 8.1$, $p = 0.005$). However, post hoc tests did not yield significance across groups, Wilcoxon rank-sum post hoc tests with a Bonferroni-Holm correction.

(C) Center stability is reduced in occupancy-partitioned APP-a grid cell maps. Bars indicate medians and error bars show the 25th and 75th percentile, two-way ANOVA (center—age × genotype interaction: $F(1, 163) = 10.62$, $p = 0.0014$; wall—age × genotype interaction: $F(1, 163) = 3.08$, $p = 0.081$), Wilcoxon rank-sum post hoc tests with a Bonferroni-Holm correction.

(D) Time-partitioned rate map examples for seven grid cells with the highest wall stability in each group. Wall and center scores are indicated above each partition (p1 and p2) set in black and red, respectively. Wall correlation scores remained consistently high between groups, but center correlation scores were generally lower in APP-a grid cells.

For all panels, n.s., non-significant, *$p < 0.05$, **$p < 0.01$.

See also Figure S2.

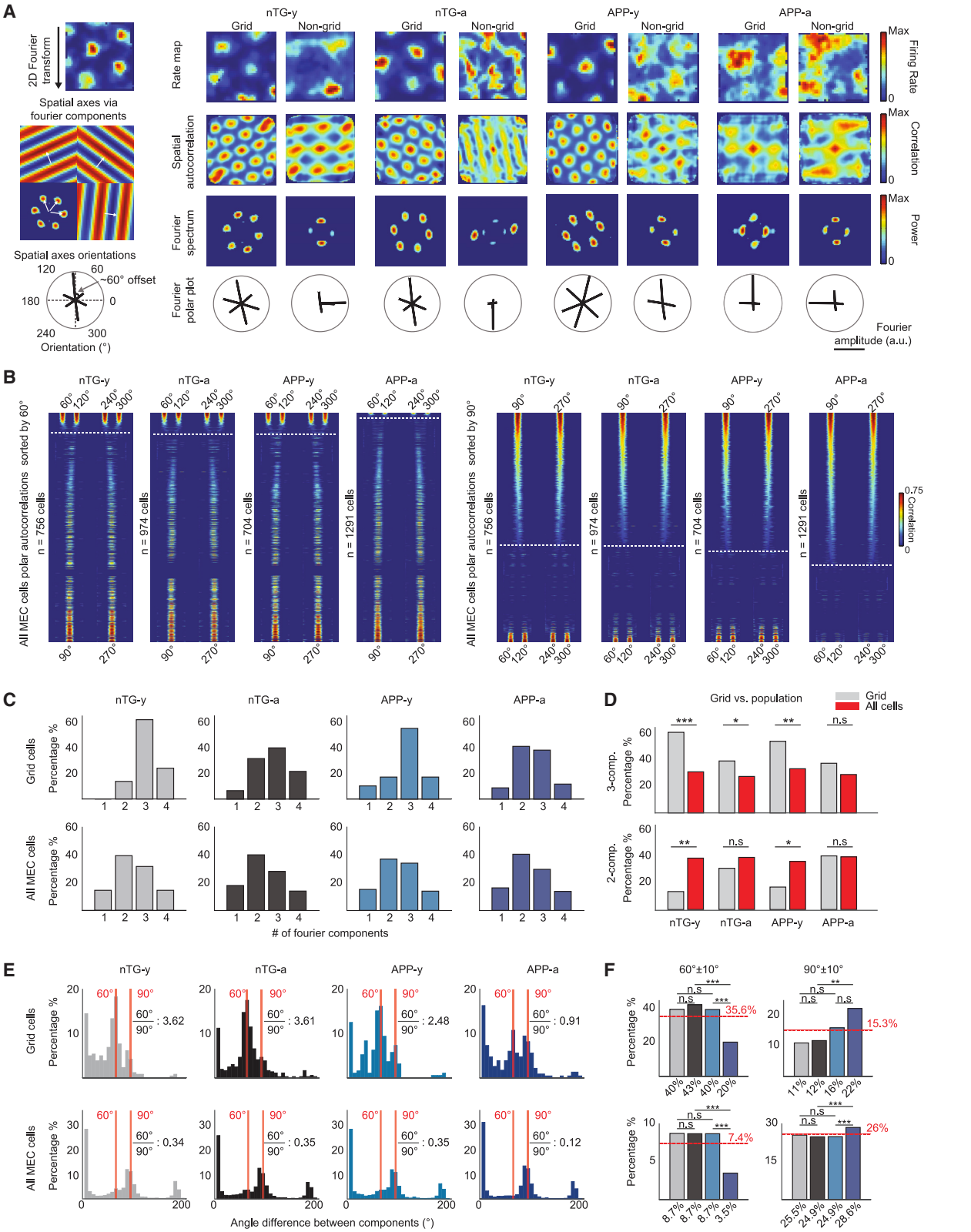

(legend on next page)

many 3-component cells were either roughly 30° or 60° hexagonally offset from the east wall (Figure 3A).[28–30] On the other hand, most 2-component cells were aligned parallel to the borders at multiples of 90° (Figure 3A). APP-a mice had ~8% more MEC cells that adopted this quadrant-like alignment profile and 5%–6% less cells that adopted hexagonal alignment profiles (Figure 3A).

Prior to visualizing the spatial alignment of grid cells, we considered the possibility that many 1- or 2-component grid cells may have been falsely classified as 3-component grid cells as a result of Fourier components not being properly identified in the Fourier spectrum due to relaxed image detection parameters. To control for this possibility, we increased image detection thresholds to obtain an additional 29% (4/14 cells), 54% (14/26 cells), 46% (6/13 cells), and 33% (9/27 cells) 3-component grid cells from 1- and 2-component grid cells in nTG-y, nTG-a, APP-y, and APP-a mice, respectively (STAR Methods; Figure S3B). From this corrected dataset, we observed that all groups had 30° and 60° 3-component grid cells or 90° 1- and 2-component grid cells (Figure 3B). Specifically, we found that 28% (10/36 cells), 19% (12/64 cells), 23% (7/30 cells), and 46% (17/37 cells) of 1- and 2-component grid cells aligned parallel to the borders in nTG-y, nTG-a, APP-y, and APP-a mice, respectively. APP-a mice had ~20%–25% more 1- and 2-component grid cells than other groups (Figure 3B). Compared with the expected distribution (the average of observed percentages across all groups), only APP-a mice had a significantly greater percentage of 1- and 2-component grid cells (Figure 3B; Table S2; binomial test: $p = 0.01$). Polar autocorrelations revealed that ~75% of grid cells were modulated at 60° intervals in nTG-y, nTG-a, and APP-y mice, whereas ~25% of cells were modulated at 90° intervals (Figure 3C). In contrast, APP-a grid cells were roughly equally split between 60° and 90° modulation (Figure 3C). Notably, 3-component grid cells had higher gridness scores than their 1- and 2-component counterparts in all groups (Figure 3C).

Together, these results provide novel insights regarding our previously reported finding of disrupted grid cell hexagonal symmetry in APP-a mice.[12] There, APP-a grid cell firing appeared random, without any clear spatially periodic structure, suggestive of increased random noise in the network or an aperiodic distribution of grid field locations. Our Fourier results, on the other hand, reveal that disrupted APP-a grid spatial periodicity is instead predominantly caused by a higher concentration of firing aligned parallel to the geometric borders. We confirmed that our results were not artifacts caused by the parameters of our correction threshold to retrieve 3-component grid cells or the square dimensionality of rate map images (Figures S4A–S4E; Table S3). Lastly, it was previously reported that grid axes were offset by ~7.5° from the reference axes of a hexagonal configuration.[30] To determine whether this coding property was present in our data, we calculated the angular offset of each Fourier component from its reference axis and found that the median angular offsets were not far off from 7.5° in all groups (Figure S4F; nTG-y: 8°, nTG-a: 6.57°, APP-y: 10.28°, APP-a: 7.14°).

Adult APP grid cells exhibit reduced theta modulation and positional coding via theta phase precession

Given the importance of theta rhythmicity for grid cell spatial coding[31,32] and entorhinal head direction and speed coding,[33,34] as well as the proposed link between entorhinal or hippocampal theta rhythms and various forms of self-motion that include running speed, positive acceleration, and vestibular inputs,[15,35–43] we examined whether intrinsic theta rhythmicity of spiking was reduced in APP-a grid cells. Visualization of the spike-time autocorrelations of 3-component grid cells revealed weaker overall theta modulation than other groups (Figure 4A). In contrast, theta modulation of 1- and 2-component grid cells did not appear to vary between groups (Figure 4A; although we note that this interpretation could be biased by smaller sample sizes).

Visualization of the power spectrums of the spike-time autocorrelations yielded a similar conclusion. APP-a 3-component grid cells showed weaker theta modulation around 8–10 Hz compared with other groups, whereas 1- and 2-component grid cells were unaffected between groups (Figure 4B). Next, we quantified the percentages of theta-modulated grid cells from the power spectrums of the spike-time autocorrelations (STAR Methods section theta modulation analyses). There were ~30%–40% less theta-modulated APP-a 3-component grid cells than other groups, but the percentages of 1- and 2-component grid cells were similar across groups (Figure 4C; hexagonal: nTG-y: 81%, nTG-a: 83%, APP-y: 78%, APP-a: 45%; quadrant-like: nTG-y: 40%, nTG-a: 50%, APP-y: 29%, APP-a: 47%). We repeated our quantifications in an unbiased manner for a wide range of temporal bin sizes between 1 and 10 ms and observed a consistent ~30%–40% reduction in

Figure 2. Adult APP MEC neurons more frequently adopt quadrant-like spatial alignment

(A) A two-dimensional (2D) Fourier transform decomposes the rate map into a small number of Fourier components. Each grid cell component can be visualized as an image of grid axes typically oriented at multiples of 60°. The orientations of all Fourier components could be visualized as a polar plot. Single grid and non-grid spatially periodic cell examples are shown for all groups.

(B) Polar autocorrelations for all MEC cells sorted by the strength of hexagonal modulation at 60° multiples or by the strength of quadrant-like modulation at 90° multiples. Dashed white lines indicate where hexagonal modulation or quadrant-like modulation ends.

(C) Percentage distribution of cells that had one-to-four Fourier components for grid cells and all MEC cells.

(D) The percentages of grid cells that had either three (one-tailed t test for proportions) or two components (two-tailed t test for proportions) vs. all MEC cells.

(E) Histograms show the distribution of angle difference between neighboring components of grid and all MEC cells. Solid red lines mark specific orientations.

(F) Bar graphs show the percentages of angular differences at 60° ± 10° and 90° ± 10° for grid cells and all MEC cells, chi-squared tests of independence (grid cells—60° instances: $\chi^2(3) = 34.94$, $p = 1.26 \times 10^{-7}$; 90° instances: $\chi^2(3) = 16.84$, $p = 7.62 \times 10^{-4}$; all MEC cells—60° instances: $\chi^2(3) = 175.96$, $p = 6.56 \times 10^{-38}$; 90° instances: $\chi^2(3) = 26.55$, $p = 7.33 \times 10^{-6}$). One-tailed t test for proportions, post hoc tests with a Bonferroni-Holm correction. Dotted red lines mark the average percentages across groups.

For all panels, n.s., non-significant, *$p < 0.05$, **$p < 0.01$, ***$p < 0.001$.

See also Figure S3.

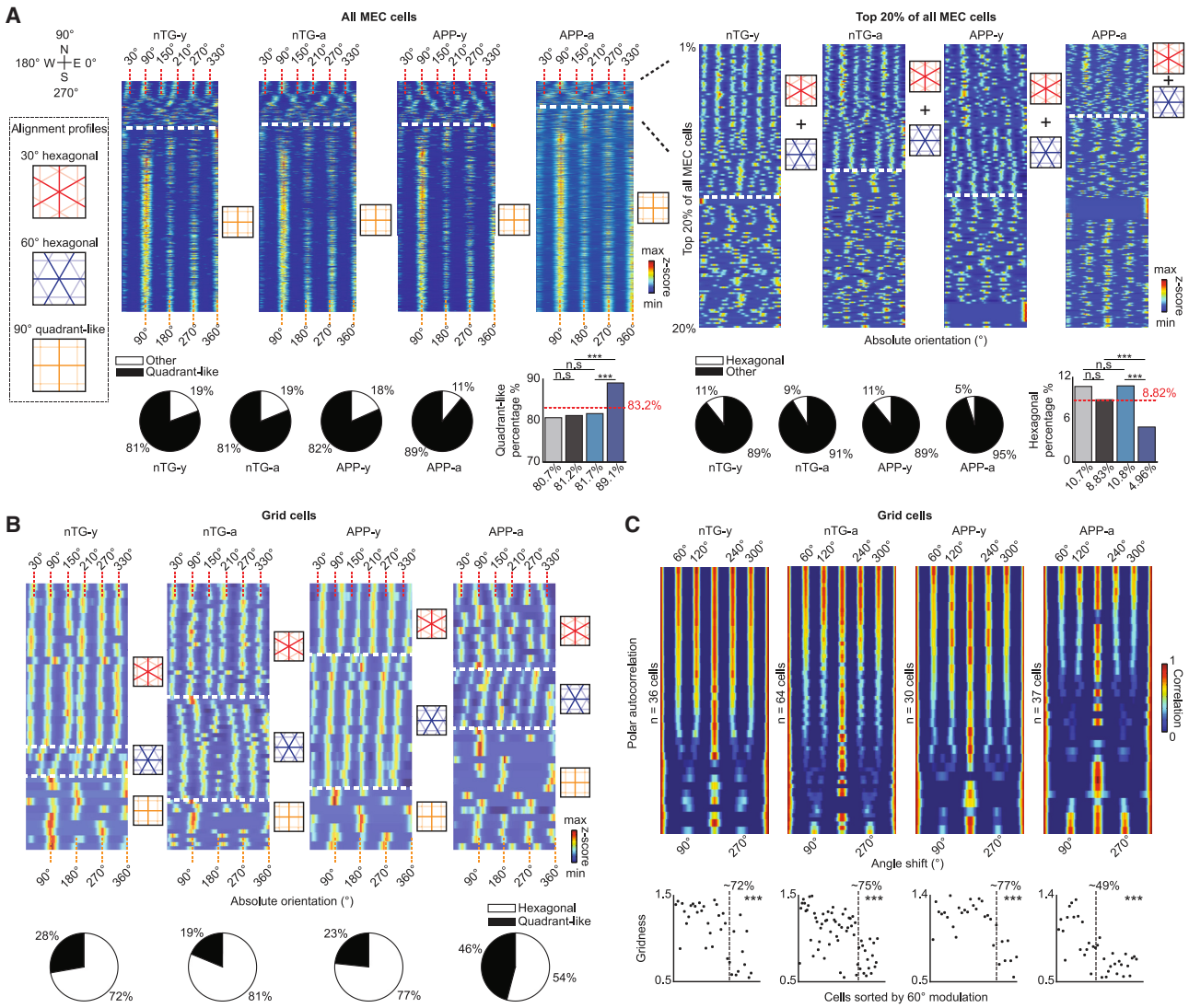

Figure 3. Adult APP grid cells align parallel to the borders

(A) Most MEC cells adopted one of three possible alignment profiles. 30° or 60° hexagonal alignments involve the first grid cell axis (obtained from the Fourier spectrum) being offset by either 30° or 60° from the east wall. Other non-grid MEC cells mostly adopted 60° quadrant-like alignment where the spatial axes aligned parallel to the borders at multiples of 90°. (Left, top) Absolute orientation of all cells relative to the recording environment. Dashed white lines indicate where quadrant-like alignment starts. (Left, bottom) Percentage distributions of quadrant-like cells between groups, chi-squared test of independence ($\chi^2(3) = 39.23$, $p = 1.55 \times 10^{-8}$). One-tailed t test for proportions, post hoc tests with a Bonferroni-Holm correction. Dotted red lines mark the average percentages across groups. (Right, top) Zoomed-in view of the absolute orientations of the top 20% of cells in the left panel. Dashed white lines indicate where 30° or 60° hexagonal alignment ends. Note that the dashed white lines in these right panels (top 20% of all MEC cells) do not indicate the exact locations marked by the dashed white lines in the left panels (all MEC cells). Between the pure hexagonal grid cells and the pure quadrant-like cells are a smaller subset of cells with uncharacterized spatial alignment profiles. (Right, bottom) Percentage distributions of hexagonal cells between groups, chi-squared test of independence ($\chi^2(3) = 31.04$, $p = 8.33 \times 10^{-7}$). One-tailed t test for proportions, post hoc tests with a Bonferroni-Holm correction. Dotted red lines mark the average percentages across groups.
(B) Top: absolute orientation of all grid cells relative to the recording environment. Grid cells could be grouped into 30° or 60° hexagonal alignment, as well as 90° quadrant-like alignment (boundaries separated by dashed white lines). To account for differences in absolute Fourier power between cells, colors indicate the *Z* score of each polar representation. Bottom: percentage distributions of hexagonal or quadrant-like grid cells between groups, chi-squared test of independence ($\chi^2(3) = 9.03$, $p = 0.029$). One-tailed t test for proportions, post hoc tests with Bonferroni-Holm corrected p values: nTG-y vs. nTG-a: 0.30, nTG-y vs. APP-y: 0.34, APP-y vs. APP-a: 0.089, nTG-a vs. APP-a: 0.0088.
(C) Polar autocorrelation for grid cells in all groups. Grid cells are sorted by the strength of hexagonal modulation at 60° multiples. Colors indicate correlation at each degree shift along the x axis. Bottom: gridness scores of grid cells sorted by their degree of hexagonal or quadrant-like modulation (90° intervals) along the x axis. The boundary between the two categories is indicated by the gray dotted lines, and the percentage of strongly hexagonally modulated grid cells are indicated for each group. Wilcoxon rank-sum tests.
For all panels, n.s., non-significant, *p < 0.05, **p < 0.01, ***p < 0.001.
See also Figures S3 and S4 and Tables S2 and S3.

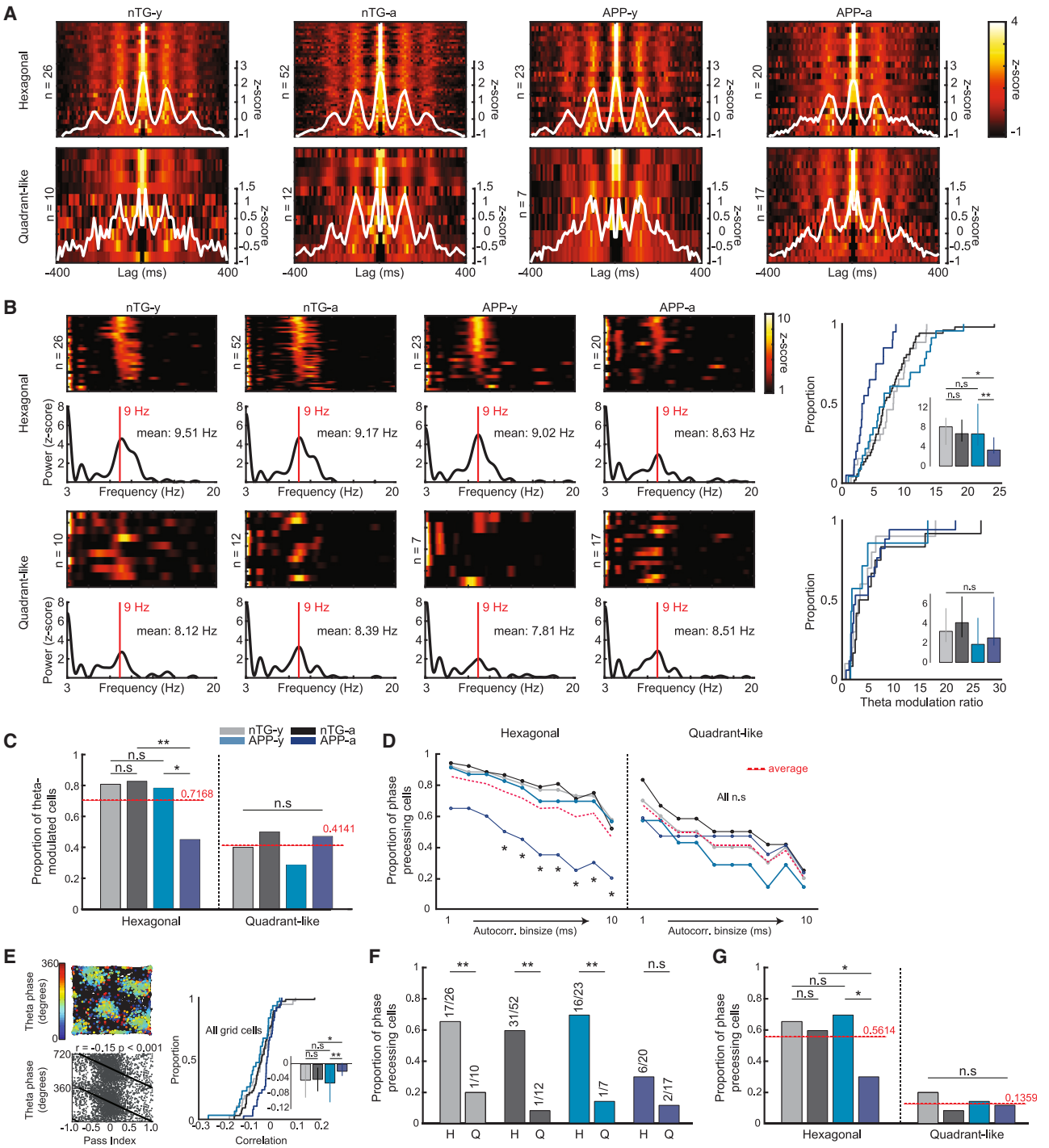

Figure 4. Adult APP grid cells have reduced theta modulation and theta phase precession

(A) Color-coded raster plots of spike-time autocorrelations for hexagonal and quadrant-like grid cells across groups. White lines are the average autocorrelation curves.

(B) Left: color-coded raster plots show the power spectrums of spike-time autocorrelations for hexagonal and quadrant-like grid cells across groups. Line graphs show the mean intrinsic frequency curve, and red lines mark a 9 Hz intrinsic frequency. Right: theta modulation ratio is reduced in APP-a grid cells. Bars indicate medians and error bars show the 25th and 75th percentile, two-way ANOVA (hexagonal—age × genotype interaction: $F(1, 117) = 6.64$, $p = 0.011$; quadrant-like—age × genotype interaction: $F(1, 42) = 0.17$, $p = 0.68$), Wilcoxon rank-sum post hoc tests with a Bonferroni-Holm correction.

(C) Proportions of significantly theta-modulated hexagonal and quadrant-like grid cells between groups, chi-squared tests of independence (hexagonal: χ^2 (3) = 11.90, $p = 0.0077$; quadrant-like: χ^2 (3) = 0.98, $p = 0.81$). One-tailed t test for proportions post hoc tests with a Bonferroni-Holm correction. Dotted red lines mark the average percentages across groups.

(legend continued on next page)

APP-a theta-modulated 3-component grid cells compared with other groups (Figure 4D).

A potential consequence of non-theta-modulated grid cells is their inability to encode distance traveled via a temporal code known as theta phase precession. As the animal travels across a firing field, a theta-modulated grid cell spikes at progressively earlier phases of theta oscillations in the local field potential.[38,39] Oscillatory interference and continuous attractor network models of grid cell firing suggest that theta phase precession properties could allow grid cells to integrate spatial displacement on the basis of self-motion, while planning future paths as part of a path integration system.[44–46] To examine theta phase precession of grid cells across groups, we computed the strength of correlation between distance traveled across a field and spike theta phase and observed an impairment in APP-a mice (Figure 4E). If theta modulation is a requirement for theta phase precession, then APP-a 3-component grid cells would logically exhibit less phase precession than other groups. Indeed, further quantification revealed that there were ~30%–40% less phase-precessing APP-a 3-component grid cells than other groups, but phase-precessing 1- and 2-component grid cells remained equally low across all groups (Figures 4F and 4G; hexagonal: nTG-y: 65%, nTG-a: 60%, APP-y: 70%, APP-a: 30%; quadrant-like: nTG-y: 10%, nTG-a: 8%, APP-y: 14%, APP-a: 12%). There was a higher proportion of phase-precessing 3-component grid cells than 1- and 2-component grid cells in nTG-y, nTG-a, and APP-y mice, but not in APP-a mice (Figure 4F). These results demonstrate that reduced grid cell theta phase precession in APP-a mice is not merely attributable to the higher proportion of 1- and 2-component grid cells but also due to the 3-component grid cells themselves being less theta rhythmic and exhibiting reduced phase precession. More broadly, these results suggest that APP-a grid cells do not reliably integrate self-motion via precisely timed theta-related mechanisms.

DISCUSSION

Our results suggest that early grid cell disruption in the J20 mouse model of amyloidopathy reflects reduced integration of self-motion cues and increased influence of environmental geometry. Reduced spatial stability toward the center suggests that grid cell impairments predominantly arise from disrupted processing of self-motion. In parallel, reduced theta modulation and theta phase precession suggests that APP-a grid cells could not properly integrate self-motion cues or accurately encode positional information within theta cycles in the local field potential. In contrast, APP-a grid cells appeared to be more strongly influenced by environmental geometry. A Fourier spectral analysis revealed that our previously reported finding of disrupted grid spatial periodicity in APP-a mice was not simply due to increased random noise or an aperiodic distribution of grid field locations[12] but directly explained by a higher concentration of spiking aligned parallel to the borders. Grid cell patterns are hypothesized to arise from intrinsic network activity and then anchor to the outside world via external landmarks.[23,24,30,47–49] The strongest grid anchor appears to be the environmental geometry itself, as different enclosure shapes affect grid cell hexagonal symmetry.[27,30,48] Future experiments should investigate whether hexagonal and quadrant-like spatial alignment profiles also persist in other types of environmental geometries that vary in polarization and symmetry. Given that grid hexagonal symmetry is disrupted in trapezoidal geometries,[27] one might intuit that MEC spatial patterns will not be as definable as those observed in a square environment. Therefore, we emphasize that the quadrant-like grid firing reported here is limited to square recording environments until there is further evidence in non-square geometries.

What are the implications for reduced theta modulation and phase precession in adult APP mice? The oscillatory interference model of grid cell firing posits that one mechanism by which grid cells integrate self-motion is interference of theta oscillations between upstream velocity-controlled oscillators (VCOs).[44,45,50] VCO firing frequencies vary according to the animal's movement speed along angular offsets of 60°. When multiple theta-modulated VCOs with preferred directions evenly spaced around 360° oscillate in phase, the thresholded sum of their directional interference patterns in a band-like manner produces grid hexagonal periodicity and theta phase precession. Alternatively, phase precession is proposed to be a "look-ahead" mechanism to plan future routes[51–53] and has been modeled in a continuous attractor network of grid cell firing.[46] Oscillatory interference and continuous attractors are distinct classes of grid cell models, but hybrid versions incorporate the main advantages of both.[54–58] Elements of both oscillatory inference and continuous attractor models could form the foundations of a path integration system that allows for continuous tracking of position along directions offset by 60° and computation of translational vectors toward

(D) Repetition of (C) when varying the bin size of the spike-time autocorrelation between 1 and 10 ms, chi-squared tests of independence (hexagonal chi-squared p values [left to right]: 0.0046, 0.027, 0.022, 0.0052, 0.0077, 0.0029, 0.0017, 0.0014, 0.0027, 0.042; quadrant-like chi-squared p values [left to right]: 0.51, 0.76, 0.91, 0.91, 0.81, 0.81, 0.81, 0.66, 0.94, 0.95). One-tailed t test for proportions, post hoc tests with a Bonferroni-Holm correction. Dotted red lines mark the average percentages across groups. Stars indicate conditions where post hoc tests revealed a significant decrease in theta-modulated grid cells in APP-a mice compared with other groups.

(E) Left: open field phase precession for an example grid cell. Trajectory of mouse in black with overlaid color-coded circles indicate the location and theta phase of spiking. Pass index values of −1 and +1 represent the entry and exit of a firing field, respectively. Right: the strength of correlation between the spiking phase and distance traveled across a firing field is reduced in APP-a mice. Data include quadrant-like and hexagonal grid cells. Bars indicate medians, and error bars show the 25th and 75th percentile, two-way ANOVA (age × genotype interaction: $F(1, 163) = 5.34$, $p = 0.02$), Wilcoxon rank-sum post hoc tests with a Bonferroni-Holm correction.

(F) Proportion of significantly phase-precessing grid cells within group. One-tailed t test for proportions.

(G) Proportions of significantly phase-precessing hexagonal and quadrant-like grid cells between groups, chi-squared tests of independence (hexagonal: $\chi^2(3) = 8.33$, $p = 0.04$; quadrant-like: $\chi^2(3) = 0.19$, $p = 0.98$). One-tailed t test for proportions post hoc tests with a Bonferroni-Holm correction. Dotted red lines mark the average percentages across groups.

For all panels except for (D), n.s., non-significant, *$p < 0.05$, **$p < 0.01$.

goal locations. For instance, neural network implementations of grid cells can be successfully trained to produce vector-based navigation by utilizing phase precession properties.[59] Specifically, the phase difference relationships of different grid cells encoding current and goal locations can accurately produce goal-directed translational vectors in large-scale two-dimensional spaces.[59] The lack of phase precession in many APP-a grid cells could impair their ability to integrate self-motion and plan future paths in the environment's center,[60,61] thus causing the grid cell network to adopt quadrant-like alignment that may integrate spatial displacement through other means, such as contact with environmental borders. The sequential organization of grid cell spikes within continuous theta cycles might also constitute a temporal readout of movement direction within short time windows.[62] Theta phase precession suggests that past grid fields fire at earlier phases in a theta cycle, while recent grid fields fire at later phases. Each theta cycle therefore describes past, current, and future locations. This continuous phase code could underlie the animal's ability to infer position relative to a starting location when path integrating across long behavioral timescales. Phase precession has also been reported in other species, including bats and humans, suggesting that phase coding serves a broad role in linking sequential locations and events.[63,64]

Our results at the neural level complement numerous studies that propose that path integration performance is a sensitive behavioral marker of early AD. It was shown that amnestic mild cognitive impairment (MCI) patients could not path integrate in the triangle completion task (TCT)—a task commonly used to assess path integration performance in human subjects.[7,65] Moreover, path integration performance in the TCT not only distinguished MCI patients from healthy control subjects but also positively correlated with increased levels of AD biomarkers, including cerebrospinal fluid levels of amyloid and total tau.[66] In further support of path integration performance as an early cognitive marker, midlife path integration impairments in the TCT were found to occur prior to cognitive impairments in other domains, such as episodic memory, visual short-term memory binding, verbal narrative recall, and non-path-integration spatial behaviors.[13] In addition to MCI and midlife, path integration, performance was impaired in *APOE ε4* carriers (the main genetic risk factor for sporadic AD[67]) as young as 18 years of age.[9,10,68] Interestingly, young *APOE ε4* carriers also preferred to navigate along the borders of a virtual arena while avoiding the center, perhaps because they could not effectively integrate self-motion cues.[10] This observation may directly relate to our finding that APP-a grid cells were spatially unstable in the environmental center. To date, clinical AD interventional trials have been largely unsuccessful, in part because the initial stages of pathology are difficult to identify, such that therapeutics are administered too late.[7,69] Although amyloid, tau, and neurodegeneration are detectable *in vivo* up to decades preceding the onset of cognitive impairments,[70] these biomarkers cannot diagnose AD in the clinic, which still relies on cognitive assessments.[71–73] Our results suggest that grid cell impairments are predominantly driven by the animal's inability to integrate self-motion cues, thereby further justifying the implementation of path integration paradigms in the clinic as a much-needed sensitive cognitive marker of early AD.

Many real-world and virtual human path integration behavioral paradigms eliminate or control against the use of environmental borders.[9,13,65,66,74–76] Partial or complete removal of external borders could force preclinical individuals to rely on self-motion information, which they have difficulty integrating, thus leading to unstable and compromised fMRI grid-like signals.[7,9,10,13] Hexagonal and quadrant-like alignment may suggest general principles about how one encodes position via self-motion. Hexagonal structure is superior to quadrant-like structure in terms of angular resolution and sampling frequency between vertices.[77] In the context of path integration, 60° grid axes allow for more frequent updating of heading direction, as well as spatial displacement or movement speed between intersection points. These advantages may explain why grid cells in general adopt hexagonal symmetry, or why grid-like representations are modulated at 60° and not at 90° intervals.[78]

The entorhinal cortex is among the initial regions affected by AD pathology[79] and contains many spatially modulated cells that we previously believed could underlie spatial navigation impairments in AD patients.[2,3,22] Our results expand the scope of circuit-level AD research beyond the entorhinal-hippocampal circuit and suggest that early AD pathology may occur in brain regions important for integrating self-motion cues—one of these regions being the anterior thalamus.[80,81] In post-mortem AD brains, extracellular amyloid is found in almost all thalamic nuclei, whereas neurofibrillary changes are most prominent in the anterior thalamic nuclei (ATN). In rodents, the ATN contain a wide population of head-direction cells and provide an important head-direction signal to the MEC.[15,82] Upstream of the ATN, head-direction cells are also found in the lateral mammillary nuclei (LMN) and dorsal tegmental nucleus (DTN).[83,84] Besides head-direction cells, the LMN and DTN contain cells that fire in response to the animal's heading velocity and pitch.[83,84] It seems counterintuitive to investigate these thalamic regions, given that we previously did not report any preferred firing direction impairments in MEC head-direction cells in APP mice.[12] However, the MEC receives strong visual inputs from the visual cortices and the postsubiculum, which may have compensated for potential deficits in self-motion integration by MEC head-direction cells.[85–87] In contrast, thalamic head-direction coding receives direct projections from vestibular nuclei and is less dependent on visual inputs provided by descending cortical projections to the thalamus.[85,86] By extension, these brainstem vestibular nuclei may also be worth investigating during early pathology, given that the supragenual nucleus (SGN) and the nucleus prepositus hypoglossi (NPH), the latter being an oculomotor system, have been proposed to relay vestibular inputs from the medial vestibular nucleus (MVN).[88,89] Non-vestibular nuclei that integrate motor-related cues also project to the head-direction system and could be susceptible to early pathology.[90] The habenula and interpeduncular nucleus (IPN) contain cells whose firing rates correlate with the animal's running speed and are presumably necessary for head-direction coding.[91,92] Our results are limited by the recording apparatus, which does not explicitly dissociate the environmental borders from the animal's self-motion. Future investigations of spatial coding in AD mouse models should therefore aim to distinguish the relative contributions of different self-motion modalities to impaired grid cell coding and path integration performance.

Tauopathy and amyloidopathy are pathological hallmarks of AD.[79,93] Although tauopathy is generally regarded as the main driver of entorhinal dysfunction in the general population,[79,94–97] different tau and Aβ mouse models independently show a shared disruption of grid cell hexagonal symmetry during early and late pathogenesis.[12,98–100] In a two-dimensional continuous attractor neural network model of grid cell activity, simulated AD synaptic damage resulting from the propagation of neurofibrillary tau tangles disrupted grid cell hexagonal symmetry.[101] Similar to APP-a mice, simulated healthy grid cells had three significant Fourier components offset by 60°. In contrast, simulated damaged grid cells had two, one, or no components, depending on the magnitude of synaptic impairment. The similarities between these model simulations of tau propagation and our experimental results in an amyloid mouse model suggest that despite the different molecular pathways of tauopathy and amyloidopathy, the loss of grid hexagonal symmetry across multiple AD mouse models might initially occur through a similar process, where the grid map detaches from the individual's self-motion while staying anchored to the external world. More broadly, our findings support existing theories that suggest that disrupted processing of self-motion by grid cells underlies path integration impairments reported during early AD.[7,9,10,12,13,66]

STAR★METHODS

Detailed methods are provided in the online version of this paper and include the following:

- KEY RESOURCES TABLE
- RESOURCE AVAILABILITY
  - Lead contact
  - Materials availability
  - Data and code availability
- EXPERIMENTAL MODEL AND SUBJECT DETAILS
  - Mice
- METHOD DETAILS
  - Surgery
  - Neural Recordings
  - Histology
  - Spike sorting
  - Position, direction, velocity estimation, and rate map construction
  - Gridness score
  - Directionality
  - Grid cell selection
  - Spatial stability analysis
  - Generation of Fourier spectrums
  - Identifying Fourier components
  - Fourier polar representations and autocorrelations
  - Fourier wavelength identification
  - Fourier orientation offset from reference axes
  - Theta modulation analyses
  - Phase precession
  - Genotyping
- QUANTIFICATION AND STATISTICAL ANALYSIS
  - Quantification of neural data
  - Statistical analysis

SUPPLEMENTAL INFORMATION

Supplemental information can be found online at https://doi.org/10.1016/j.cub.2023.04.065.

ACKNOWLEDGMENTS

We graciously thank S. Kim, Z. Ante, K. Harandian, Q. He, A. Ismailova, D. Patel, A. Zhen, and A. Milette-Gagnon for their assistance in experiments. We also thank A.T. Keinath, H.C. Yong, J.Q. Lee, J.C. Robinson, and M. Oulé for providing helpful comments on prior versions of the manuscript, as well as all members of the Brandon laboratory for helpful discussions. This work was funded by CIHR project grants #367017 and #377074, an NSERC discovery grant #74105, a Scottish Rite Charitable Foundation grant, a Canada Fund for Innovation grant, and a Canada Research Chairs award to M.P.B. This work was also supported by the German Research Foundation (DFG) project YO177/7-1 and YO177/8-1 to M.Y. J.Y. is supported by a doctoral training grant from the Fonds de recherche du Québec and previously by a master's training grant from the Fonds de recherche du Québec and a CIHR master's training fellowship.

AUTHOR CONTRIBUTIONS

J.Y., A.R., M.Y., and M.P.B. conceived the project and wrote the manuscript. J.Y. conducted all experiments. J.Y. and A.R. conducted analysis of data.

DECLARATION OF INTERESTS

The authors declare no competing interests.

Received: March 2, 2023
Revised: April 20, 2023
Accepted: April 27, 2023
Published: May 22, 2023

REFERENCES

1. Fyhn, M., Molden, S., Witter, M.P., Moser, E.I., and Moser, M.-B. (2004). Spatial representation in the entorhinal cortex. Science *305*, 1258–1264.
2. Hafting, T., Fyhn, M., Molden, S., Moser, M.-B., and Moser, E.I. (2005). Microstructure of a spatial map in the entorhinal cortex. Nature *436*, 801–806.
3. Jacobs, J., Weidemann, C.T., Miller, J.F., Solway, A., Burke, J.F., Wei, X.-X., Suthana, N., Sperling, M.R., Sharan, A.D., Fried, I., et al. (2013). Direct recordings of grid-like neuronal activity in human spatial navigation. Nat. Neurosci. *16*, 1188–1190.
4. Gil, M., Ancau, M., Schlesiger, M.I., Neitz, A., Allen, K., De Marco, R.J., and Monyer, H. (2018). Impaired path integration in mice with disrupted grid cell firing. Nat. Neurosci. *21*, 81–91.
5. McNaughton, B.L., Battaglia, F.P., Jensen, O., Moser, E.I., and Moser, M.-B. (2006). Path integration and the neural basis of the "cognitive map.". Nat. Rev. Neurosci. *7*, 663–678.
6. Mittelstaedt, M.-L., and Mittelstaedt, H. (1980). Homing by path integration in a mammal. Naturwissenschaften *67*, 566–567.
7. Segen, V., Ying, J., Morgan, E., Brandon, M., and Wolbers, T. (2022). Path integration in normal aging and Alzheimer's disease. Trends Cogn. Sci. *26*, 142–158.
8. Coughlan, G., Laczó, J., Hort, J., Minihane, A.-M., and Hornberger, M. (2018). Spatial navigation deficits - overlooked cognitive marker for preclinical Alzheimer disease? Nat. Rev. Neurol. *14*, 496–506.
9. Bierbrauer, A., Kunz, L., Gomes, C.A., Luhmann, M., Deuker, L., Getzmann, S., Wascher, E., Gajewski, P.D., Hengstler, J.G., Fernandez-Alvarez, M., et al. (2020). Unmasking selective path integration deficits in Alzheimer's disease risk carriers. Sci. Adv. *6*, eaba1394.
10. Kunz, L., Schröder, T.N., Lee, H., Montag, C., Lachmann, B., Sariyska, R., Reuter, M., Stirnberg, R., Stöcker, T., Messing-Floeter, P.C., et al.

(2015). Reduced grid-cell-like representations in adults at genetic risk for Alzheimer's disease. Science *350*, 430–433.

11. Mucke, L., Masliah, E., Yu, G.Q., Mallory, M., Rockenstein, E.M., Tatsuno, G., Hu, K., Kholodenko, D., Johnson-Wood, K., and McConlogue, L. (2000). High-level neuronal expression of abeta 1–42 in wild-type human amyloid protein precursor transgenic mice: synaptotoxicity without plaque formation. J. Neurosci. *20*, 4050–4058.
12. Ying, J., Keinath, A.T., Lavoie, R., Vigneault, E., El Mestikawy, S., and Brandon, M.P. (2022). Disruption of the grid cell network in a mouse model of early Alzheimer's disease. Nat. Commun. *13*, 886.
13. Newton, C., Pope, M., Rua, C., Henson, R., Ji, Z., Burgess, N., Rodgers, C.T., Stangl, M., Dounavi, M.-E., Castegnaro, A., et al. (2023). Path integration selectively predicts midlife risk of Alzheimer's disease. https://doi.org/10.1101/2023.01.31.526473.
14. Winter, S.S., Mehlman, M.L., Clark, B.J., and Taube, J.S. (2015). Passive transport disrupts grid signals in the parahippocampal cortex. Curr. Biol. *25*, 2493–2502.
15. Winter, S.S., Clark, B.J., and Taube, J.S. (2015). Spatial navigation. Disruption of the head direction cell network impairs the parahippocampal grid cell signal. Science *347*, 870–874.
16. Chen, G., Manson, D., Cacucci, F., and Wills, T.J. (2016). Absence of visual input results in the disruption of grid cell firing in the mouse. Curr. Biol. *26*, 2335–2342.
17. Kraus, B.J., Brandon, M.P., Robinson, R.J., 2nd, Connerney, M.A., Hasselmo, M.E., and Eichenbaum, H. (2015). During running in place, grid cells integrate elapsed time and distance run. Neuron *88*, 578–589.
18. Pérez-Escobar, J.A., Kornienko, O., Latuske, P., Kohler, L., and Allen, K. (2016). Visual landmarks sharpen grid cell metric and confer context specificity to neurons of the medial entorhinal cortex. eLife *5*, e16937. https://doi.org/10.7554/eLife.16937.
19. Campbell, M.G., Ocko, S.A., Mallory, C.S., Low, I.I.C., Ganguli, S., and Giocomo, L.M. (2018). Principles governing the integration of landmark and self-motion cues in entorhinal cortical codes for navigation. Nat. Neurosci. *21*, 1096–1106.
20. Chen, G., Lu, Y., King, J.A., Cacucci, F., and Burgess, N. (2019). Differential influences of environment and self-motion on place and grid cell firing. Nat. Commun. *10*, 630.
21. Kropff, E., Carmichael, J.E., Moser, M.-B., and Moser, E.I. (2015). Speed cells in the medial entorhinal cortex. Nature *523*, 419–424.
22. Sargolini, F., Fyhn, M., Hafting, T., McNaughton, B.L., Witter, M.P., Moser, M.-B., and Moser, E.I. (2006). Conjunctive representation of position, direction, and velocity in entorhinal cortex. Science *312*, 758–762.
23. Buetfering, C., Allen, K., and Monyer, H. (2014). Parvalbumin interneurons provide grid cell-driven recurrent inhibition in the medial entorhinal cortex. Nat. Neurosci. *17*, 710–718.
24. Couey, J.J., Witoelar, A., Zhang, S.-J., Zheng, K., Ye, J., Dunn, B., Czajkowski, R., Moser, M.-B., Moser, E.I., Roudi, Y., et al. (2013). Recurrent inhibitory circuitry as a mechanism for grid formation. Nat. Neurosci. *16*, 318–324.
25. Miao, C., Cao, Q., Moser, M.-B., and Moser, E.I. (2017). Parvalbumin and somatostatin interneurons control different space-coding networks in the medial entorhinal cortex. Cell *171*, 507–521.e17.
26. Barry, C., Hayman, R., Burgess, N., and Jeffery, K.J. (2007). Experience-dependent rescaling of entorhinal grids. Nat. Neurosci. *10*, 682–684.
27. Krupic, J., Bauza, M., Burton, S., Barry, C., and O'Keefe, J. (2015). Grid cell symmetry is shaped by environmental geometry. Nature *518*, 232–235.
28. Krupic, J., Burgess, N., and O'Keefe, J. (2012). Neural representations of location composed of spatially periodic bands. Science *337*, 853–857.
29. Stensola, H., Stensola, T., Solstad, T., Frøland, K., Moser, M.-B., and Moser, E.I. (2012). The entorhinal grid map is discretized. Nature *492*, 72–78.
30. Stensola, T., Stensola, H., Moser, M.-B., and Moser, E.I. (2015). Shearing-induced asymmetry in entorhinal grid cells. Nature *518*, 207–212.
31. Brandon, M.P., Bogaard, A.R., Libby, C.P., Connerney, M.A., Gupta, K., and Hasselmo, M.E. (2011). Reduction of theta rhythm dissociates grid cell spatial periodicity from directional tuning. Science *332*, 595–599.
32. Koenig, J., Linder, A.N., Leutgeb, J.K., and Leutgeb, S. (2011). The spatial periodicity of grid cells is not sustained during reduced theta oscillations. Science *332*, 592–595.
33. Brandon, M.P., Bogaard, A.R., Schultheiss, N.W., and Hasselmo, M.E. (2013). Segregation of cortical head direction cell assemblies on alternating θ cycles. Nat. Neurosci. *16*, 739–748.
34. Hinman, J.R., Brandon, M.P., Climer, J.R., Chapman, G.W., and Hasselmo, M.E. (2016). Multiple running speed signals in medial entorhinal cortex. Neuron *91*, 666–679.
35. Maurer, A.P., Vanrhoads, S.R., Sutherland, G.R., Lipa, P., and McNaughton, B.L. (2005). Self-motion and the origin of differential spatial scaling along the septo-temporal axis of the hippocampus. Hippocampus *15*, 841–852.
36. Terrazas, A., Krause, M., Lipa, P., Gothard, K.M., Barnes, C.A., and McNaughton, B.L. (2005). Self-motion and the hippocampal spatial metric. J. Neurosci. *25*, 8085–8096.
37. Jeewajee, A., Barry, C., O'Keefe, J., and Burgess, N. (2008). Grid cells and theta as oscillatory interference: electrophysiological data from freely moving rats. Hippocampus *18*, 1175–1185.
38. Hafting, T., Fyhn, M., Bonnevie, T., Moser, M.-B., and Moser, E.I. (2008). Hippocampus-independent phase precession in entorhinal grid cells. Nature *453*, 1248–1252.
39. O'Keefe, J., and Recce, M.L. (1993). Phase relationship between hippocampal place units and the EEG theta rhythm. Hippocampus *3*, 317–330.
40. Skaggs, W.E., McNaughton, B.L., Wilson, M.A., and Barnes, C.A. (1996). Theta phase precession in hippocampal neuronal populations and the compression of temporal sequences. Hippocampus *6*, 149–172.
41. Kropff, E., Carmichael, J.E., Moser, E.I., and Moser, M.-B. (2021). Frequency of theta rhythm is controlled by acceleration, but not speed, in running rats. Neuron *109*, 1029–1039.e8.
42. Jacob, P.-Y., Poucet, B., Liberge, M., Save, E., and Sargolini, F. (2014). Vestibular control of entorhinal cortex activity in spatial navigation. Front. Integr. Neurosci. *8*, 38.
43. Ravassard, P., Kees, A., Willers, B., Ho, D., Aharoni, D.A., Cushman, J., Aghajan, Z.M., and Mehta, M.R. (2013). Multisensory control of hippocampal spatiotemporal selectivity. Science *340*, 1342–1346.
44. Burgess, N. (2008). Grid cells and theta as oscillatory interference: theory and predictions. Hippocampus *18*, 1157–1174.
45. Burgess, N., Barry, C., and O'Keefe, J. (2007). An oscillatory interference model of grid cell firing. Hippocampus *17*, 801–812.
46. Navratilova, Z., Giocomo, L.M., Fellous, J.-M., Hasselmo, M.E., and McNaughton, B.L. (2012). Phase precession and variable spatial scaling in a periodic attractor map model of medial entorhinal grid cells with realistic after-spike dynamics. Hippocampus *22*, 772–789.
47. Gardner, R.J., Lu, L., Wernle, T., Moser, M.-B., and Moser, E.I. (2019). Correlation structure of grid cells is preserved during sleep. Nat. Neurosci. *22*, 598–608.
48. Stensola, T., and Moser, E.I. (2016). Grid cells and spatial maps in entorhinal cortex and hippocampus. In Research and Perspectives in Neurosciences Research and Perspectives in Neurosciences (Springer International Publishing), pp. 59–80.
49. Trettel, S.G., Trimper, J.B., Hwaun, E., Fiete, I.R., and Colgin, L.L. (2019). Grid cell co-activity patterns during sleep reflect spatial overlap of grid fields during active behaviors. Nat. Neurosci. *22*, 609–617.
50. Hasselmo, M.E., and Brandon, M.P. (2008). Linking cellular mechanisms to behavior: entorhinal persistent spiking and membrane potential oscillations may underlie path integration, grid cell firing, and episodic memory. Neural Plast. *2008*, 658323.

51. Tsodyks, M.V., Skaggs, W.E., Sejnowski, T.J., and McNaughton, B.L. (1996). Population dynamics and theta rhythm phase precession of hippocampal place cell firing: a spiking neuron model. Hippocampus *6*, 271–280.

52. Wallenstein, G.V., and Hasselmo, M.E. (1997). GABAergic modulation of hippocampal population activity: sequence learning, place field development, and the phase precession effect. J. Neurophysiol. *78*, 393–408.

53. Hasselmo, M.E., and Eichenbaum, H. (2005). Hippocampal mechanisms for the context-dependent retrieval of episodes. Neural Netw. *18*, 1172–1190.

54. Hasselmo, M.E., and Brandon, M.P. (2012). A model combining oscillations and attractor dynamics for generation of grid cell firing. Front. Neural Circuits *6*, 30.

55. Schmidt-Hieber, C., and Häusser, M. (2013). Cellular mechanisms of spatial navigation in the medial entorhinal cortex. Nat. Neurosci. *16*, 325–331.

56. Domnisoru, C., Kinkhabwala, A.A., and Tank, D.W. (2013). Membrane potential dynamics of grid cells. Nature *495*, 199–204.

57. Bush, D., and Burgess, N. (2014). A hybrid oscillatory interference/continuous attractor network model of grid cell firing. J. Neurosci. *34*, 5065–5079.

58. Bush, D., and Schmidt-Hieber, C. (2018). Computational Models of Grid Cell Firing. In Springer Series in Computational Neuroscience (Springer International Publishing), pp. 585–613.

59. Bush, D., Barry, C., Manson, D., and Burgess, N. (2015). Using grid cells for navigation. Neuron *87*, 507–520.

60. Erdem, U.M., and Hasselmo, M. (2012). A goal-directed spatial navigation model using forward trajectory planning based on grid cells. Eur. J. Neurosci. *35*, 916–931.

61. Erdem, U.M., and Hasselmo, M.E. (2014). A biologically inspired hierarchical goal directed navigation model. J. Physiol. Paris *108*, 28–37.

62. Zutshi, I., Leutgeb, J.K., and Leutgeb, S. (2017). Theta sequences of grid cell populations can provide a movement-direction signal. Curr. Opin. Behav. Sci. *17*, 147–154.

63. Eliav, T., Geva-Sagiv, M., Yartsev, M.M., Finkelstein, A., Rubin, A., Las, L., and Ulanovsky, N. (2018). Nonoscillatory phase coding and synchronization in the bat hippocampal formation. Cell *175*, 1119–1130.e15.

64. Qasim, S.E., Fried, I., and Jacobs, J. (2021). Phase precession in the human hippocampus and entorhinal cortex. Cell *184*, 3242–3255.e10.

65. Mokrisova, I., Laczo, J., Andel, R., Gazova, I., Vyhnalek, M., Nedelska, Z., Levcik, D., Cerman, J., Vlcek, K., and Hort, J. (2016). Real-space path integration is impaired in Alzheimer's disease and mild cognitive impairment. Behav. Brain Res. *307*, 150–158.

66. Howett, D., Castegnaro, A., Krzywicka, K., Hagman, J., Marchment, D., Henson, R., Rio, M., King, J.A., Burgess, N., and Chan, D. (2019). Differentiation of mild cognitive impairment using an entorhinal cortex-based test of virtual reality navigation. Brain *142*, 1751–1766.

67. Liu, C.-C., Liu, C.-C., Kanekiyo, T., Xu, H., and Bu, G. (2013). Apolipoprotein E and Alzheimer disease: risk, mechanisms and therapy. Nat. Rev. Neurol. *9*, 106–118.

68. Coughlan, G., Coutrot, A., Khondoker, M., Minihane, A.-M., Spiers, H., and Hornberger, M. (2019). Toward personalized cognitive diagnostics of at-genetic-risk Alzheimer's disease. Proc. Natl. Acad. Sci. USA *116*, 9285–9292.

69. Panza, F., Lozupone, M., Logroscino, G., and Imbimbo, B.P. (2019). A critical appraisal of amyloid-β-targeting therapies for Alzheimer disease. Nat. Rev. Neurol. *15*, 73–88.

70. Jack, C.R., Jr., Knopman, D.S., Jagust, W.J., Petersen, R.C., Weiner, M.W., Aisen, P.S., Shaw, L.M., Vemuri, P., Wiste, H.J., Weigand, S.D., et al. (2013). Tracking pathophysiological processes in Alzheimer's disease: an updated hypothetical model of dynamic biomarkers. Lancet Neurol. *12*, 207–216.

71. McKhann, G.M., Knopman, D.S., Chertkow, H., Hyman, B.T., Jack, C.R., Jr., Kawas, C.H., Klunk, W.E., Koroshetz, W.J., Manly, J.J., Mayeux, R., et al. (2011). The diagnosis of dementia due to Alzheimer's disease: recommendations from the National Institute on Aging-Alzheimer's Association workgroups on diagnostic guidelines for Alzheimer's disease. Alzheimers Dement. *7*, 263–269.

72. Albert, M.S., DeKosky, S.T., Dickson, D., Dubois, B., Feldman, H.H., Fox, N.C., Gamst, A., Holtzman, D.M., Jagust, W.J., Petersen, R.C., et al. (2011). The diagnosis of mild cognitive impairment due to Alzheimer's disease: recommendations from the National Institute on Aging-Alzheimer's Association workgroups on diagnostic guidelines for Alzheimer's disease. Alzheimers Dement. *7*, 270–279.

73. Jack, C.R., Jr., Bennett, D.A., Blennow, K., Carrillo, M.C., Dunn, B., Haeberlein, S.B., Holtzman, D.M., Jagust, W., Jessen, F., Karlawish, J., et al. (2018). NIA-AA Research Framework: toward a biological definition of Alzheimer's disease. Alzheimers Dement. *14*, 535–562.

74. Allen, G.L., Kirasic, K.C., Rashotte, M.A., and Haun, D.B.M. (2004). Aging and path integration skill: kinesthetic and vestibular contributions to wayfinding. Percept. Psychophys. *66*, 170–179.

75. Mahmood, O., Adamo, D., Briceno, E., and Moffat, S.D. (2009). Age differences in visual path integration. Behav. Brain Res. *205*, 88–95.

76. Stangl, M., Kanitscheider, I., Riemer, M., Fiete, I., and Wolbers, T. (2020). Sources of path integration error in young and aging humans. Nat. Commun. *11*, 2626.

77. Mersereau, R.M. (1979). The processing of hexagonally sampled two-dimensional signals Proceedings of the IEEE Inst. Electr. Proc. IEEE *67*, 930–949.

78. Doeller, C.F., Barry, C., and Burgess, N. (2010). Evidence for grid cells in a human memory network. Nature *463*, 657–661.

79. Braak, H., and Braak, E. (1991). Neuropathological stageing of Alzheimer-related changes. Acta Neuropathol. *82*, 239–259.

80. Braak, H., and Braak, E. (1991). Alzheimer's disease affects limbic nuclei of the thalamus. Acta Neuropathol. *81*, 261–268.

81. Aggleton, J.P., Pralus, A., Nelson, A.J.D., and Hornberger, M. (2016). Thalamic pathology and memory loss in early Alzheimer's disease: moving the focus from the medial temporal lobe to Papez circuit. Brain *139*, 1877–1890.

82. Taube, J.S. (1995). Head direction cells recorded in the anterior thalamic nuclei of freely moving rats. J. Neurosci. *15*, 70–86.

83. Stackman, R.W., and Taube, J.S. (1998). Firing properties of rat lateral mammillary single units: head direction, head pitch, and angular head velocity. J. Neurosci. *18*, 9020–9037.

84. Bassett, J.P., and Taube, J.S. (2001). Neural correlates for angular head velocity in the rat dorsal tegmental nucleus. J. Neurosci. *21*, 5740–5751.

85. Yoder, R.M., Clark, B.J., and Taube, J.S. (2011). Origins of landmark encoding in the brain. Trends Neurosci. *34*, 561–571.

86. Clark, B.J., and Taube, J.S. (2012). Vestibular and attractor network basis of the head direction cell signal in subcortical circuits. Front. Neural Circuits *6*, 7.

87. Ajabi, Z., Keinath, A.T., Wei, X.-X., and Brandon, M.P. (2023). Population dynamics of head-direction neurons during drift and reorientation. Nature *615*, 892–899.

88. Clark, B.J., Brown, J.E., and Taube, J.S. (2012). Head direction cell activity in the anterodorsal thalamus requires intact supragenual nuclei. J. Neurophysiol. *108*, 2767–2784.

89. Butler, W.N., and Taube, J.S. (2015). The nucleus prepositus hypoglossi contributes to head direction cell stability in rats. J. Neurosci. *35*, 2547–2558.

90. Stackman, R.W., Golob, E.J., Bassett, J.P., and Taube, J.S. (2003). Passive transport disrupts directional path integration by rat head direction cells. J. Neurophysiol. *90*, 2862–2874.

91. Sharp, P.E., Turner-Williams, S., and Tuttle, S. (2006). Movement-related correlates of single cell activity in the interpeduncular nucleus and habenula of the rat during a pellet-chasing task. Behav. Brain Res. *166*, 55–70.

92. Clark, B.J., Sarma, A., and Taube, J.S. (2009). Head direction cell instability in the anterior dorsal thalamus after lesions of the interpeduncular nucleus. J. Neurosci. *29*, 493–507.

93. Berron, D., Vogel, J.W., Insel, P.S., Pereira, J.B., Xie, L., Wisse, L.E.M., Yushkevich, P.A., Palmqvist, S., Mattsson-Carlgren, N., Stomrud, E., et al. (2021). Early stages of tau pathology and its associations with functional connectivity, atrophy and memory. Brain *144*, 2771–2783.

94. Archetti, D., Ingala, S., Venkatraghavan, V., Wottschel, V., Young, A.L., Bellio, M., Bron, E.E., Klein, S., Barkhof, F., Alexander, D.C., et al. (2019). Multi-study validation of data-driven disease progression models to characterize evolution of biomarkers in Alzheimer's disease. NeuroImage Clin. *24*, 101954.

95. Johnson, K.A., Schultz, A., Betensky, R.A., Becker, J.A., Sepulcre, J., Rentz, D., Mormino, E., Chhatwal, J., Amariglio, R., Papp, K., et al. (2016). Tau positron emission tomographic imaging in aging and early Alzheimer disease. Ann. Neurol. *79*, 110–119.

96. Ossenkoppele, R., Schonhaut, D.R., Schöll, M., Lockhart, S.N., Ayakta, N., Baker, S.L., O'Neil, J.P., Janabi, M., Lazaris, A., Cantwell, A., et al. (2016). Tau PET patterns mirror clinical and neuroanatomical variability in Alzheimer's disease. Brain *139*, 1551–1567.

97. Young, A.L., Oxtoby, N.P., Daga, P., Cash, D.M., Fox, N.C., Ourselin, S., Schott, J.M., and Alexander, D.C.; Alzheimer's Disease Neuroimaging Initiative (2014). A data-driven model of biomarker changes in sporadic Alzheimer's disease. Brain *137*, 2564–2577.

98. Fu, H., Rodriguez, G.A., Herman, M., Emrani, S., Nahmani, E., Barrett, G., Figueroa, H.Y., Goldberg, E., Hussaini, S.A., and Duff, K.E. (2017). Tau pathology induces excitatory neuron loss, grid cell dysfunction, and spatial memory deficits reminiscent of early Alzheimer's disease. Neuron *93*, 533–541.e5.

99. Jun, H., Bramian, A., Soma, S., Saito, T., Saido, T.C., and Igarashi, K.M. (2020). Disrupted place cell remapping and impaired grid cells in a knockin model of Alzheimer's disease. Neuron *107*, 1095–1112.e6.

100. Ridler, T., Witton, J., Phillips, K.G., Randall, A.D., and Brown, J.T. (2020). Impaired speed encoding and grid cell periodicity in a mouse model of tauopathy. eLife *9*, e59045, https://doi.org/10.7554/eLife.59045.

101. Zhi, Y., and Cox, D. (2021). Neurodegenerative damage reduces firing coherence in a continuous attractor model of grid cells. Phys. Rev. E *104*, 044414.

102. Nagahara, A.H., Mateling, M., Kovacs, I., Wang, L., Eggert, S., Rockenstein, E., Koo, E.H., Masliah, E., and Tuszynski, M.H. (2013). Early BDNF treatment ameliorates cell loss in the entorhinal cortex of APP transgenic mice. J. Neurosci. *33*, 15596–15602.

103. Hong, S., Beja-Glasser, V.F., Nfonoyim, B.M., Frouin, A., Li, S., Ramakrishnan, S., Merry, K.M., Shi, Q., Rosenthal, A., Barres, B.A., et al. (2016). Complement and microglia mediate early synapse loss in Alzheimer mouse models. Science *352*, 712–716.

104. Wright, A.L., Zinn, R., Hohensinn, B., Konen, L.M., Beynon, S.B., Tan, R.P., Clark, I.A., Abdipranoto, A., and Vissel, B. (2013). Neuroinflammation and neuronal loss precede Aβ plaque deposition in the hAPP-J20 mouse model of Alzheimer's disease. PLoS One *8*, e59586.

105. Saganich, M.J., Schroeder, B.E., Galvan, V., Bredesen, D.E., Koo, E.H., and Heinemann, S.F. (2006). Deficits in synaptic transmission and learning in amyloid precursor protein (APP) transgenic mice require C-terminal cleavage of APP. J. Neurosci. *26*, 13428–13436.

106. Verret, L., Mann, E.O., Hang, G.B., Barth, A.M.I., Cobos, I., Ho, K., Devidze, N., Masliah, E., Kreitzer, A.C., Mody, I., et al. (2012). Inhibitory interneuron deficit links altered network activity and cognitive dysfunction in Alzheimer model. Cell *149*, 708–721.

107. Palop, J.J., Chin, J., Roberson, E.D., Wang, J., Thwin, M.T., Bien-Ly, N., Yoo, J., Ho, K.O., Yu, G.-Q., Kreitzer, A., et al. (2007). Aberrant excitatory neuronal activity and compensatory remodeling of inhibitory hippocampal circuits in mouse models of Alzheimer's disease. Neuron *55*, 697–711.

108. Cheng, I.H., Scearce-Levie, K., Legleiter, J., Palop, J.J., Gerstein, H., Bien-Ly, N., Puoliväli, J., Lesné, S., Ashe, K.H., Muchowski, P.J., et al. (2007). Accelerating amyloid-beta fibrillization reduces oligomer levels and functional deficits in Alzheimer disease mouse models. J. Biol. Chem. *282*, 23818–23828.

109. Climer, J.R., Newman, E.L., and Hasselmo, M.E. (2013). Phase coding by grid cells in unconstrained environments: two-dimensional phase precession. Eur. J. Neurosci. *38*, 2526–2541.

110. Kempter, R., Leibold, C., Buzsáki, G., Diba, K., and Schmidt, R. (2012). Quantifying circular-linear associations: hippocampal phase precession. J. Neurosci. Methods *207*, 113–124.

STAR★METHODS

KEY RESOURCES TABLE

REAGENT or RESOURCE	SOURCE	IDENTIFIER
Chemicals, peptides, and recombinant proteins		
Isoflurane	Baxter	SKU: FDG9623
Heparin	Sandoz	DIN: 02303086
Paraformaldehyde	MilliporeSigma	CAS Number: 30525-89-4
Sucrose	MilliporeSigma	CAS Number: 57-50-1
2-methylbutane	Fisher Scientific	CAS Number: 78-78-4
DAPI containing Fluoromount-G	SouthernBiotech	Catalog Number: 0100-20
REDExtract-N-Amp™ Tissue PCR Kit	MilliporeSigma	EC Number: 254-457-8
Deposited data		
Positional and spike data	This paper	https://github.com/johnson-ying/Code-for-Ying-et-al.-2023/
Experimental models: Organisms/strains		
Mouse: APP mice: B6.Cg-Zbtb20 Tg(PDGFB-APPSwInd) 20Lms/2Mmjax	The Jackson Laboratory	MMRRC Stock No: 34836-JAX
Software and algorithms		
Neuralynx recording software	Neuralynx	https://neuralynx.com/software/cheetah
Plexon offline sorter	Plexon	https://plexon.com/products/offline-sorter/
MATLAB	MathWorks	https://www.mathworks.com/products/matlab.html
Custom MATLAB code	This paper	https://github.com/johnson-ying/Code-for-Ying-et-al.-2023/
Other		
Versadrive	Custom built	N/A
Tetrode wire	Nichrome	https://www.amazon.com/Sandvik-Precision-Fine-Tetrode-Feet/dp/B0062MNUG6
Digital Neuralynx recording system	Neuralynx	Digital Lynx 4SX
Cryostat	Leica	Model: Leica CM3050 S
QIAxcel instrument	Qiagen	QIAxcel Advanced
Slide scanner	Olympus	Model: VS120

RESOURCE AVAILABILITY

Lead contact

Further information and requests for resources and reagents should be directed to and will be fulfilled by the lead contact, Mark P. Brandon (mark.brandon@mcgill.ca).

Materials availability

This study did not generate new unique reagents.

Data and code availability

All data reported in this paper and original code are available at https://github.com/johnson-ying/Code-for-Ying-et-al.-2023/ and are publicly available as of the date of publication. DOIs are listed in the key resources table. Any additional information required to re-analyze the data reported in this paper is available from the lead contact upon request.

EXPERIMENTAL MODEL AND SUBJECT DETAILS

Mice

J20 APP male mice (B6.Cg-Zbtb20 Tg(PDGFB-APPSwInd) 20Lms/2Mmjax) were obtained from The Jackson Laboratory (MMRRC stock #34836) and bred with female C57/BL6/j mice. Mice were individually housed on a 12-h light/dark cycle and underwent experiments during the light cycle. Housing room conditions of the mice were maintained at 20-22 degrees Celsius and 21-30% humidity.

All experimental procedures were performed in accordance with McGill University and Douglas Hospital Research Centre Animal Use and Care Committee (protocol #2015-7725) and in accordance with Canadian Institutes of Health Research guidelines.

J20 mice undergo progressive neuronal loss in layers 2, 3 and 5 of the MEC. By 7.5 months of age, all layers exhibit a total loss of 16.3% of neurons compared to control mice, along with reduced density of presynaptic terminals by 7 months of age.[102] By 6 months of age, region CA1 of the hippocampus also experiences 10%+ of neuronal loss compared to control mice. In parallel, marker-immunoreactivity and electron microscopy confirm the presence of synapse loss in the CA1 as early as 3 months. Besides neuronal and synaptic loss, the complement-dependent pathway and microglia are upregulated in a manner that is dependent on soluble Aβ oligomeric levels in the hippocampus.[103] On a related note, gliosis (activated astrocytes) and neuroinflammation (activated microglia) are elevated across age in the hippocampus by 6 months of age.[104] Furthermore, *in vitro* slice electrophysiology experiments reveal that basal synaptic transmission recorded in CA1 and long-term potentiation in the Schaffer collateral–CA1 synapse are impaired by 3 months of age.[105] In terms of oscillatory activity, between 4-7 months of age, gamma oscillations are reduced in the parietal cortices which causes network hypersynchrony and are linked to a reduction in the voltage-gated sodium channel subunit Nav1.1 predominantly found in parvalbumin interneurons.[106] Such hypersynchrony may be linked to spontaneous nonconvulsive seizure activity between 4-7 months, along with numerous inhibitory deficits in the dentate gyrus.[107] At the behavioral level, J20 mice exhibit numerous spatial navigation impairments in the Morris water maze, the radial arm maze and a food-foraging path integration task in darkness.[12,104,108] To examine the impact of these Aβ-mediated changes on neural coding during early pathology, we restricted our experiments between 3-7 months of age.

Single-unit recording data in the MEC were collected from 68 APP mice and non-transgenic littermates across four experimental groups: young APP mice (3-4.5 months of age), adult APP mice (4.5-7 months of age), young non-transgenic (nTG) mice (3-4.5 months of age), adult nTG mice (4.5-7 months of age). Thirty-one males and 37 females were used. Ten animals fell into multiple age groups. The male/female ratios were 6:5, 16:16, 9:5, and 11:10 for young APP, adult APP, young nTG, and adult nTG mice respectively.

METHOD DETAILS

Surgery

On the day of surgery, mice were anesthetized using isoflurane (0.5% - 3% in O_2) and administered carprofen (0.01 ml/g) subcutaneously. Three anchor screws were secured to the skull and a ground wire was positioned either above the cerebellum at midline position or the left visual cortex. A 'versadrive' containing four independently movable tetrodes (Axona, Inc) was implanted on top of the right MEC at the following stereotaxic coordinates: 3.4 mm lateral to the midline, 0.25-0.40 mm anterior to the transverse sinus. Tetrodes were gold-plated to lower impedances to 150-250 kΩ at 1 kHz prior to surgery. The versadrive was angled at eight degrees in the posterior direction. Following placement, the versadrive was secured in place using Kwik-Sil and dental acrylic. The ground wire was soldered to the implant, and tetrodes were lowered 1.0 mm from the dorsal surface of the MEC. All surgical procedures were performed in accordance with McGill University and Douglas Hospital Research Centre Animal Use and Care Committee (protocol #2015-7725) and in accordance with Canadian Institutes of Health Research guidelines.

Neural Recordings

Three days post-surgery, mice were placed on water restriction and maintained at 85% of their *ad libidum* weight throughout experiments. Mice were recorded in a 75 x 75 cm box. The box had rectangular and triangular cue cards on the north and west walls, respectively. The walls were white, their height was 30 cm, and the flooring was black. The recording box was surrounded by anti-static curtains that masked a lot of visibility of any distal landmarks in the recording room. The only polarizing distal landmark was the illumination from a lamp that shone against the west wall.

As mice explored their environments, water droplets were randomly scattered to motivate the subjects to sample the entire arena. Once mice provided good trajectory coverage, tetrodes were turned until theta rhythmic units were observed which indicated that the tetrodes had entered the MEC. Across days, tetrodes were advanced in increments of 25 microns to sample new putative MEC neurons.

To record spikes and local field potentials, versadrives were connected to a multichannel amplifier tethered to a digital Neuralynx (Bozeman, MT) recording system, and data were acquired using Cheetah 5.0 software (Neuralynx, Inc). Signals were amplified and band-pass filtered between 0.6 kHz and 6 kHz. Spike waveform thresholds were adjusted before each recording and ranged between 35-140 μV depending on unit activity. Waveforms that crossed threshold were digitized at 32 kHz and recorded across all four channels of the given tetrode. Local field potentials were recorded across all tetrodes.

See also Figure S1 and Table S1.

Histology

Animals were anesthetized with Isoflurane and perfused intracardially using saline and 4% paraformaldehyde. Animal heads were left in 4% paraformaldehyde for 24-72 hours following perfusion, before brains were extracted. Brains sanks in a 30% sucrose solution before being frozen and stored in a -80°C freezer. Sagittal brain sections (40μm) were obtained using a cryostat and Nissl-stained with a Cresyl violet solution. In cases where brain slices came off the glass slides during Nissl-staining, slices were instead mounted using a fluorescent DAPI labeling mounting medium.

Tetrode tracks were characterized to be in the superficial or deep layers based on the location of track tips. Only data collected from tetrodes within the MEC were included in analysis.

Spike sorting

Single-units were isolated 'offline' manually using Offline Sorter 2.8.8 (Plexon, Inc). Neurons were separated based on peak amplitudes and principal component measures of spike waveforms. Evaluations of the presence of biologically realistic interspike intervals, temporal autocorrelations, and cross correlations confirmed single-unit isolation. The experimenter was blind to the age and genotype of the subjects and only well-separated clusters were included in analysis.

Position, direction, velocity estimation, and rate map construction

Positional data was acquired at 30 frames per second at 720 x 480 pixel resolution (4.9 pixels per cm) using a camera purchased from Neuralynx (Bozeman, MT). The camera was elevated at a height to fully capture the entire recording arena. The estimated position of the animal was the centroid of a group of red and green diodes positioned on the recording head stage. Head direction was calculated as the angle between the red and green diodes. Up to five lost samples due to occlusion of tracking LEDs, or reflections in the environment were replaced by a linear interpolation for both position and directional data. Running velocity was calculated using a Kalman filter. Rate maps were constructed by calculating the occupancy-normalized firing rate for 3cm x 3cm bins of positional data. Data were smoothed by a two-dimensional convolution with a pseudo-Gaussian kernel involving a three pixel (9 cm) standard deviation. In most analyses (when specified), rate maps were resized into squares of size 36 x 36 pixels or 26 x 26 pixels.

Gridness score

We calculated the gridness score using the same procedure described in Brandon et al.[31] This metric quantifies hexagonal periodicity in the firing rate map, while also accounting for elliptical eccentricity along one of two mirror lines that exist in a hexagonal lattice structure. Distortion along one of the mirror lines was corrected after determining the major and minor axes of the grid based on the six closest fields to the central peak of the rate map autocorrelogram. The entire autocorrelogram was compressed so that the major axis became equal to the minor axis. Large eccentricities where the minor axis was less than half of the major axis were not corrected. From the compressed autocorrelogram, we extracted a ring of the six closest peaks to the center peak. A rotational autocorrelation of this ring was calculated to observe the periodicity in paired pixel correlations across 180 degrees of rotation. The gridness score was computed as the difference between the highest correlation observed at 30, 90, or 150 degrees of rotation and the lowest correlation observed at 60 or 120 degrees of rotation.

Directionality

The animal's head direction was collected in bins of 6 degrees and the number of spikes in each bin was divided by the time spent facing that direction. The mean resultant length (MRL) of the polar plot was taken as a metric of directional selectivity.

Grid cell selection

Grid cells were determined via a shuffling procedure. Spike trains from each neuron were randomly shifted in time by at least 30 seconds. We then calculated the gridness scores of each neuron. This process was repeated 50 times for each neuron, and the 99th percentile of the resulting distribution of scores was determined as the significance criteria. This resulted in a gridness threshold of 0.54. Cells that passed this threshold were characterized as grid cells.

Spatial stability analysis

Time-partitioned analysis: Rate maps of size 26 x 26 pixels were created for each grid cell. The first 30 minutes of each recording was divided into two 15-minute partitions. Each rate map was divided into wall or center regions, depending on how many pixel layers each had. Next, the pixels corresponding to both regions were extracted for both partitions. A Pearson correlation was computed for wall or center time partitions.

Occupancy-partitioned analysis: A 26 x 26 pixel matrix (an 'occupancy map') tracked the number of time frames that the animal spent in each spatial bin throughout the full recording. All time frames where the mouse was stationary (velocity < 5cm/s) were dropped. The values in each bin were then halved, and the resulting numbers represented the number of time frames per bin allocated to each partition. Time frames were then selected throughout the entire recording session in an 'ascending' or 'monotonically increasing' manner to build both partition maps. Rate maps of size 26 x 26 pixels were created for each partition. The rest of the analysis was the same as the time-partitioned analysis.

Generation of Fourier spectrums

We followed the procedure used previously in Krupic et al.[28,78] We used the fft2 MATLAB function to compute the two-dimensional Fourier transform of the rate map of a given cell. Initial rate maps were unsmoothed at size 36 x 36 pixels and center zero-padded to have size 256 x 256 pixels in order to increase the spatial resolution of the Fourier spectrogram. After running fft2 on the zero-padded rate map, the resulting amplitude spectrum was divided by the mean firing rate of the given cell to allow for comparison between cells that have different firing rates. The amplitude spectrum was element-wise squared to re-visualize the spectrum in the power domain.

We used the fftshift MATLAB function to shift low frequencies to the center and high frequencies to the periphery of the spectrum. Lastly, we created a two-dimensional gaussian loss function (where the bump values are 0) with a width of 1. This gaussian was centered at the strongest value pixel of the spectrum and element-wise multiplied. This procedure was done to erase the center block of energy that resulted from the fft2 function.

Identifying Fourier components

The Fourier power spectrum was first computed. To reduce effects of noise, the 75th percentile value of power in shuffled data (from the Voronoi procedure described in Krupic et al.[28,83]) was subtracted and negative values set to zero. To further control for noise, values lower than 25% of the resulting maximum power were also set to zero. These are higher thresholds than what was used by Krupic et al.[28,84] However, to ensure that these thresholds do not bias our results, we varied this latter parameter in Table S3.

A zero matrix with the size of the Fourier spectrum was created. Any non-zero value in the corrected Fourier spectrum had its corresponding position in the zero matrix set to 1. Using the regionprops MATLAB function, Fourier components were individually identified as separate "regions". To account for effects of noise, any regions with an area less than 10 pixels was discarded. Similar to Krupic et al.,[28] cells with more than 4 Fourier components were not included in analysis.[86]

To determine a component's orientation, the distances (along the x- and y-axes) between the centroids of each region and the center of the Fourier spectrum were computed. The "wave vector" corresponding to the x- and y-displacements were calculated as:

$$k_x = \frac{2\pi * dx}{Nb}$$

$$k_y = \frac{2\pi * dy}{Mb}$$

Where dx and dy are the x- and y-displacements, respectively; N and M are the x- and y-axis lengths of the rate map (both 36 in our case); b is the bin size in meters (0.0208 in our data). The orientation of the wave vector was:

$$\varphi = atan\left(\frac{k_y}{k_x}\right)$$

And the orientation of the periodic band (or grid axes) is 90 degrees offset to the wave vector's orientation.

$$\theta = \varphi + 90^{\circ}$$

Fourier polar representations and autocorrelations

To compute Fourier polar representations, we first plotted the orientations of individual Fourier components on a polar plot. The power corresponding to each orientation was that given component's Fourier power in the Fourier spectrum. The polar plot was then smoothed using a one-dimensional Gaussian kernel with a standard deviation of 13 degrees.

To compute Fourier polar autocorrelations, the smoothed polar plots were circularly shifted 360 degrees. At each degree shift, the Pearson correlation between the original and shifted polar profiles was computed.

Fourier wavelength identification

To compute a Fourier component's wavelength, a line was drawn over the Fourier spectrum at the given component's orientation. This was achieved using the improfile MATLAB function, which draws a line between a specific start (the Fourier spectrum's center) and end point (a point exceeding the dimensions of the spectrum) on a given image (the spectrum). The distance away from the spectrum's center along this line which had the maximum Fourier power was taken as the wavelength.

Fourier orientation offset from reference axes

A grid cell was first determined to be either a 30° or 60° hexagonal grid, or a 90° quadrant-like grid based on where the Fourier orientations faced. The reference axes for a 30° grid faced (30°, 90°, 150°, 210°, 270°, 330°). The reference axes for a 60° grid faced (0°, 60°, 120°, 180°, 240°, 300°). The reference axes for a 90° grid faced (0°, 90°, 180°, 270°). The angular difference between each Fourier component and its closest reference axis was calculated as the offset.

Theta modulation analyses

To visualize theta modulation, spike-time autocorrelations were computed for each cell with 5ms temporal bins from a lag of -400 to 400ms. The resulting autocorrelations were convolved with a 25ms gaussian and z-score normalized. The average z-scored correlation curve for all cells was also plotted.

To compute intrinsic frequency, the spike-time autocorrelations were zero padded to 2^13 samples and the power spectrum was calculated using the Chronux toolbox function MTSPECTRUMC from Matlab. The intrinsic frequency of a given cell was taken as the frequency with the max power in the 6-12 Hz range. The theta modulation ratio was calculated as the mean power within 6-12 Hz, divided by the mean power between all other frequencies within 2-100 Hz. To be considered a significantly theta-modulated cell, the

mean power within 6-12 Hz needed to be four times greater than the mean power within 2-100 Hz (a theta modulation ratio greater than 4).

Phase precession

The degree of grid cell phase precession was calculated via a 'pass index' analysis as described in Climer et al.[109] Briefly, this method quantifies precession by assessing the correlation of a cell's firing in relation with theta phase as the mouse passes a spatial field. The spatial field locations were estimated using a 'field index' method that calculates the degree of occupancy-normalized firing within each bin of positional data. Field contours and centers were then generated by using various parameters involving the field index and firing rate. Lastly, based on the field index signal across a recording session, a mouse's entry and exit of a spatial field could be estimated. The pass index was therefore determined by normalizing field index signal segments consisting of the passage across a spatial field between -1 and +1, where -1 represents the start of a pass, 0 represents the center, and +1 represents the end. Phase of spiking across field crossing was aligned to this normalized position and a linear-circular correlation was computed between field index and spiking phase.[110] A grid cell with a significant correlation at $p < 0.05$ and a slope per pass between -1440 and -22 was classified as a phase-precessing cell.

Genotyping

Tail samples were collected at weaning for genotyping, and also prior to brain perfusion. DNA samples were extracted and amplified using REDExtract-N-Amp™ Tissue PCR Kit (MilliporeSigma, XNAT-100RXN) and the primer sequence and PCR protocol from The Jackson Laboratory (MMRRC, 34836-JAX). Genotyping results were visualized with a QIAxcel instrument (Qiagen).

QUANTIFICATION AND STATISTICAL ANALYSIS

Quantification of neural data

Single-unit data were obtained using Neuralynx (Bozeman, MT) software and isolated 'offline' manually using graphical cluster cutting software (Plexon, Inc) individually for each recording session. Custom MATLAB scripts were used to analyze neural data.

Statistical analysis

Statistical analyses for neural and behavioral data were performed using MATLAB. Bars in bar graphs involving continuous data represent median values, and the error bars represent the 25th and 75th percentile.

Comparisons between two groups involving continuous data used unpaired, two-tailed Wilcoxon rank sum tests. Comparisons between more than two groups involving continuous data used a two-way ANOVA with age and genotype as the factors. A significant interaction effect was followed by post-hoc testing using unpaired, two-tailed Wilcoxon rank sum tests with a Bonferroni-Holm correction in the following four comparisons: nTG-y vs. nTG-a, nTG-y vs APP-y, APP-y vs. APP-a, nTG-a vs. APP-a.

Comparisons between more than two groups involving proportion data used a chi-squared test of independence. A significant interaction effect was followed by post-hoc testing using one-tailed t-tests for proportions with a Bonferroni-Holm correction in the following four comparisons: nTG-y vs. nTG-a, nTG-y vs APP-y, APP-y vs. APP-a, nTG-a vs. APP-a.

Figure 2D used a one-tailed t-test for proportions to compare 3-component cells, and a two-tailed t-test for proportions to compare 2-component cells.

In addition to a chi-squared test, Figure 3B also used a binomial test. A binomial test determines the probability of an outcome when there are only two possible outcomes. In our case, the test determined if the obtained proportion by a group was equal or unequal (either lesser or larger) compared to expected chance. Expected chance was calculated as the average of the proportions obtained in all four groups. The rationale for calculating expected chance in this manner is assuming that all four animal groups were the same age and genotype, then the average of the four should provide a theoretical level of chance.

All statistical tests used an alpha value of 0.05. Significance was determined as follows: * $p < 0.05$, ** $p < 0.01$,*** $p < 0.001$.